AIAA SciTech Forum
11–15 & 19–21 January 2021, VIRTUAL EVENT
AIAA Scitech 2021 Forum

10.2514/6.2021-1322

Characterization of the Aerodynamics of Rectangular Cylinders with Surface Topology

Kian Kalan*, Alireza Safaripour†, Ahmed M. Naguib‡ and Manoochehr M. Koochesfahani§
Michigan State University, East Lansing, Michigan, 48824

The main motivation behind this study is to understand the susceptibility of the suspension lines of Precision Airdrop Systems (PADS) to flow-induced vibrations by galloping instability. Such vibrations are undesirable as they negatively affect the controllability of PADS. Suspension cables of PADS have a cross-section of a round-corner rectangle with surface geometrical features (topology) produced by the braided structure of the cables. Therefore, an experimental study is conducted to provide fundamental understanding of the effects of surface topology on the instability of round-corner rectangular cylinders to galloping. The study utilizes a baseline cylinder with smooth (topology-free) surface, a side (chord-to-width) ratio of 2.5 and fully-round corners. Results from the baseline model are compared against those from cylinders with the same geometry but with added surface topology. Fourier modes are employed to define different surface topologies with an amplitude of 5% of the cylinder width d along the perimeter only (2D geometry), as well as along the span (3D geometry). Boundary-layer-resolved measurements are conducted using single-component molecular tagging velocimetry at Reynolds numbers based on d of $Re_d = 1,100$ and $2,500$, and cylinder angle of attack of $0°, 2°$ and $5°$. A complementary investigation using direct force measurements is also carried out to determine the galloping stability characteristics of the cylinders examined. Results suggest that the topology could lead to destabilization to galloping when the associated geometrical features cause the flow to separate along the corner region of the cylinder, promoting earlier separation relative to the baseline smooth geometry. On the other hand, reattachment of the separated shear layer, which has a stabilizing effect on galloping, is promoted by the presence of spanwise topology variation (3D geometry) and increasing Re_d.

I. Nomenclature

C_D	=	drag coefficient
C_L	=	lift coefficient
C_y	=	transverse-force coefficient
c	=	cylinder chord
d	=	cylinder width
F_D	=	drag force
F_L	=	lift force
F_y	=	transverse force
l	=	cylinder span
n	=	number of surface topology wavelengths around the cylinder perimeter
P	=	cylinder perimeter
Re_d	=	width-based Reynolds number; $U_\infty d/\nu$
r	=	cylinder corner radius
s	=	coordinate along the cylinder perimeter
U_r	=	instantaneous freestream velocity relative to the cylinder
U_∞	=	freestream velocity

* Graduate Student, Mechanical Engineering, 1449 Engineering Research Ct A109, East Lansing, MI 48824, AIAA Member.
† Post-Doctoral Research Fellow, Mechanical Engineering, 1449 Engineering Research Ct A22, East Lansing, MI 48824, AIAA Member.
‡ Professor, Mechanical Engineering, 1449 Engineering Research Ct C128, East Lansing, MI 48824, AIAA Associate Fellow.
§ Professor, Mechanical Engineering, 1449 Engineering Research Ct A131, East Lansing, MI 48824, AIAA Associate Fellow.

u_{rms}	=	fluctuating-streamwise-velocity root mean square
x	=	streamwise coordinate relative to cylinder center
y	=	cross-stream coordinate relative to cylinder center
z	=	spanwise coordinate
α	=	angle of attack (AoA)
Δt	=	time difference between 1c-MTV image pair
ϵ	=	surface topology
ϵ_o	=	surface topology amplitude
λ_s	=	surface topology wavelength along the cylinder perimeter
λ_z	=	surface topology wavelength along the cylinder span
ν	=	fluid kinematic viscosity
ρ	=	fluid density

II. Introduction

Galloping is a flow-induced instability that can affect elastically-mounted non-circular structures, including rectangular cylinders, causing large-amplitude self-sustained translational oscillations of the cylinders (usually normal to the flow direction). Figure 1 illustrates a rectangular cylinder that is mounted elastically such that it can undergo an oscillatory motion in y direction due to an environmental disturbance. The oscillatory motion velocity ($\dot{y}$) will change the effective angle of attack (α) of the cylinder with time, causing unsteadiness in the lift (F_L) and drag (F_D) forces on the cylinder. The normal force coefficient in y direction (C_y) is related to the lift (C_L) and drag (C_D) coefficients through Equation 1.

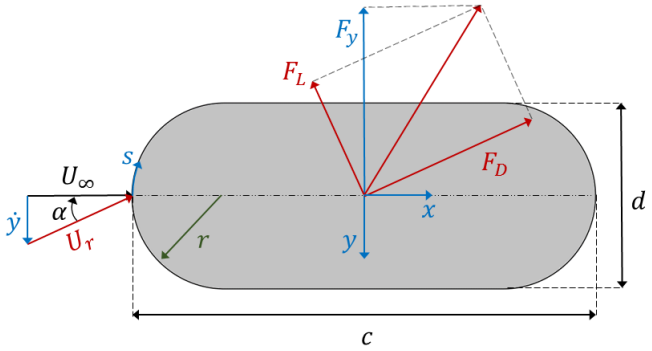

Figure 1. Schematic of cross section of a rectangular cylinder with round corners and forces acting on it upon oscillating in the transverse (y) direction.

$$C_y = \frac{F_y}{0.5\rho {U_\infty}^2 dl} = -\frac{1}{\cos^2\alpha}(C_L \cos\alpha + C_D \sin\alpha), \quad (1)$$

where,

$$C_L = \frac{F_L}{0.5\rho U_r^2 dl}, \quad (2)$$

$$C_D = \frac{F_D}{0.5\rho U_r^2 dl}. \quad (3)$$

In the above equations, U_∞ and U_r denote the steady freestream and instantaneous oncoming (relative to the moving cylinder) velocities, respectively, F_y is the transverse force, ρ is the fluid density, d is the cylinder width, and l is the cylinder span. Galloping instability can occur when the transverse force on the body increases with angle of attack, resulting in reinforcing the oscillations [1]. If the frequency of galloping is sufficiently smaller than the vortex shedding frequency of the cylinder, the flow behavior can be assumed to be quasi-steady. This assumption permits defining the main criterion for the cylinder's susceptibility to

galloping based on the variation of F_y with α for a static cylinder. More specifically, the cylinder is unstable if $\partial C_y/\partial\alpha > 0$.

When the galloping instability criterion is met, many structures with non-circular cross section, such as ice-coated power lines, bridge decks, and marine structures can experience galloping [1]. The suspension lines of Precision Airdrop Systems (PADS) have also been shown to be susceptible to galloping, which can negatively impact their controllability and performance [2]. This susceptibility is not unexpected considering the cross section of these suspension lines is typically non-circular and resembles a rectangle with round corners, similar to what is shown in Figure 1. Additionally, due to braiding, the surface of the lines is not smooth, but rather characterized by topological features [3]. Therefore, it is important to understand the effect of the surface topology of these suspension lines on their aeroelastic behavior.

In a recent work from our group [4-5], the presence of the surface topology was observed to change the galloping stability of cylinders of the same geometry as that shown in Figure 3, for Reynolds numbers $Re_d = U_\infty d/\nu$ from 1,100 to 10,000. These conclusions were made based on measurement of C_y variation with α for static cylinders in a wind tunnel. In a following study [6], we investigated some of the effects of similar surface topology on the flow field around the cylinders in a water tunnel facility at $Re_d = 2{,}500$. While the study provided significant insight into the effect of the surface topology on boundary layer separation and the near wake behavior of the flow around the cylinders, it was difficult to make direct connections with the force measurements in the wind tunnel in [4-5]. Specifically, it was not possible to ascertain that at the same Reynolds number, the $C_y - \alpha$ characteristics are the same in the wind and the water tunnel tests. The uncertainty arose from differences in: (1) the freestream turbulence level in the two facilities, (2) the cylinder-model's aspect ratio, and (3) the flow blockage by the test model.

In the present work, complementary force and velocimetry measurements are performed for the same cylinder models used in [6] in the *same* water-tunnel facility to enable making a *direct connection* between the basic flow-field characteristics and the observed changes in the $C_y - \alpha$ behavior (and hence galloping instability) due to surface topology. A second goal of the present study is to examine the Reynolds number effect on the characteristics of the flow and the force within the Reynolds number range relevant to PADS suspension lines ($1{,}000 \leq Re_d \leq 10{,}000$). Aerodynamic forces are recorded through direct force measurements, while one-component molecular tagging velocimetry (1c-MTV) is utilized to measure the streamwise velocity profiles within the boundary layer of the flow around the cylinders. These measurements are carried out for cylinders with different prescribed surface topologies (see section III) and are compared to their counterpart on a smooth-surface model.

III. Experimental Setup

The experiments are conducted in a closed-return, free-surface water tunnel (Engineering Laboratory Design, ELD) in the Turbulent Mixing and Unsteady Aerodynamics Laboratory (TMUAL) at Michigan State University. The test section dimensions are 152 mm × 152 mm × 457 mm. The models are 3D printed cylinders with a 11.4 mm-diameter stainless steel shaft inserted along their centerline to prevent warping. This shaft extends above the cylinder's span, through a skimmer plate, and is clamped to a Parker manual rotary stage (model number 2535). The Plexiglass skimmer plate, which is utilized to provide a well-defined wall boundary condition at the free surface of the test section, spans 76 mm ($5.1d$) upstream and downstream of the model's center while extending over the full tunnel width (shown in Figure 2). There is a 0.5 mm clearance between the ends of the cylinder and both the tunnel bottom surface and the skimmer plate. The streamwise position of the cylinder is such that its centerline is $13.3d$ downstream of the test section entrance. The placement of the model results in a 9.8% geometrical blockage in the test section (at $\alpha = 0°$).

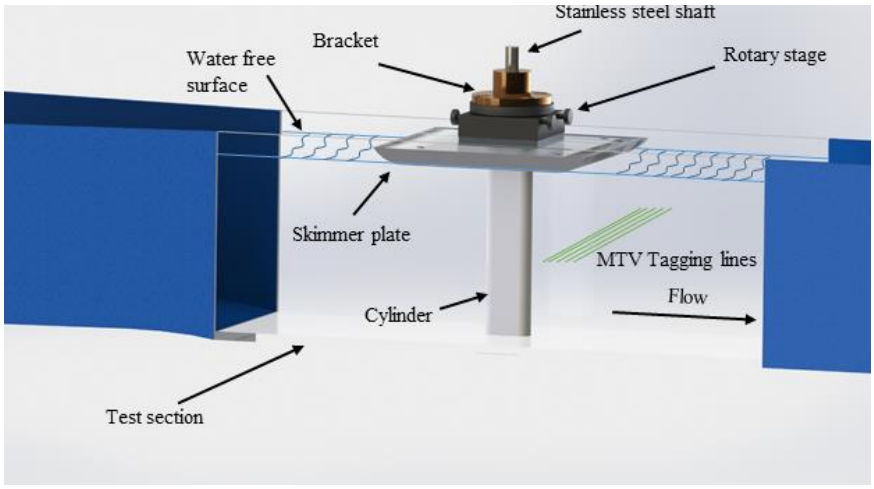

Figure 2. A 3D model of the velocimetry experimental setup in the test section.

A nominally rectangular smooth cylinder with fully-round corners and cross-sectional dimensions of d = 15 mm, c = 37.5 mm, and r = 7.5 mm (see Figure 1), corresponding to a side ratio c/d = 2.5, is used as the baseline geometry of this study. The models are 139.6 mm long and they span the full height of the test section for an aspect ratio of 9.3. Since the main motivation behind the current study is to provide a fundamental understanding (independent of specific applications) of the effects of surface topology, a mathematical expression is used to represent the surface topology, instead of an exact replica of a PADS suspension line. An advantage of this approach is that the effects of different geometrical parameters of the surface topology can be studied separately. Therefore, a two-dimensional Fourier-mode synthesis is employed to generate the surface topology ε, which is the deviation of the cylinder surface from the baseline smooth cylinder cross-section (see Figure 3):

$$\varepsilon = \frac{\varepsilon_0}{2}\left[\cos\left[2\pi\left(\frac{s}{\lambda_s} + \frac{z}{\lambda_z}\right)\right] + \cos\left[2\pi\left(\frac{s}{\lambda_s} - \frac{z}{\lambda_z}\right)\right]\right]. \quad (4)$$

In Equation 4, s and z are the coordinates along the circumference of the baseline cylinder and the spanwise direction, respectively, ε_0 is the topology amplitude, and λ_s and λ_z are the topology wavelengths in s and z directions, respectively (see Figure 3), with $\lambda_s = P/n$ and P and n represent the baseline model's perimeter and the number of topology wavelengths around the perimeter, respectively. To approximate the suspension line geometry reported in [3], the following parameters are specified for the cylinders: ε_0/d = 5%, λ_z/λ_s = 1.5, and n = 10.

To systematically study the effect of surface topology, several distinct geometries are investigated. In addition to the baseline smooth cylinder and the 3D topology (shown in Figures 1 and 3 respectively), two other models are investigated which have cross sections that are uniform along the span ($\lambda_z = \infty$, exhibiting 2D shape). The cross sections of these cylinders are similar to the cross section of the 3D model at two different spanwise planes, where one has a peak at the leading edge (LE) and the other a valley, as depicted in Figure 3 at planes A-A and B-B, respectively. This is done to distinguish the effects of the cross-sectional geometry on flow behavior from those due to shape variation along the span.

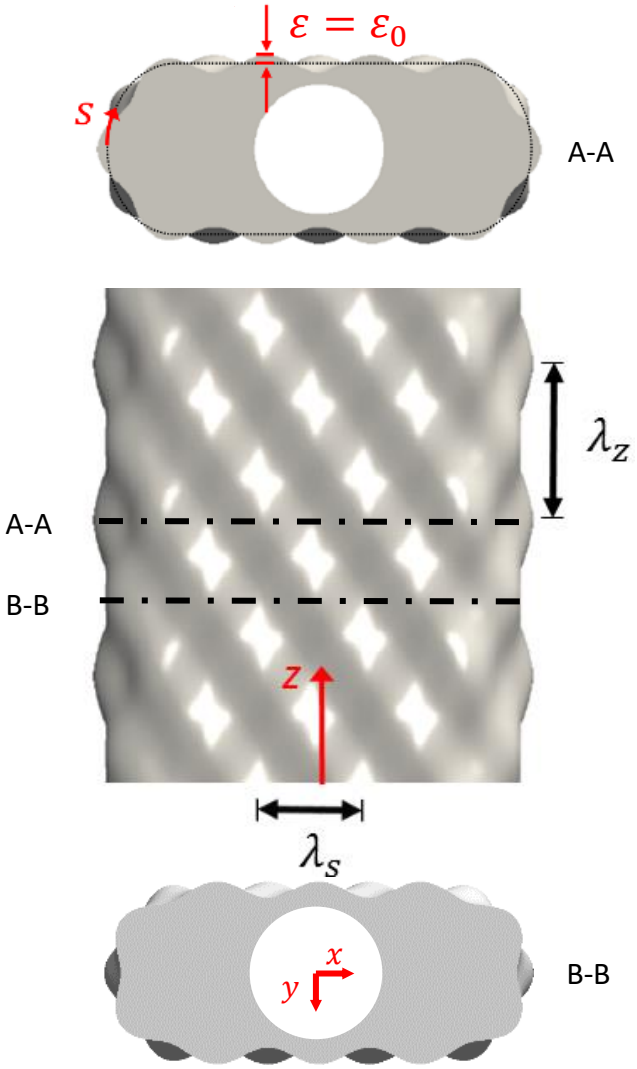

Figure 3. Top and cross-sectional views of the cylinder with $\varepsilon_0/d = 5\%, n = 10, and\ \lambda_z\ /\lambda_s = 1.5$.

The present work employs one-component molecular tagging velocimetry (1c-MTV), which is a whole-field non-intrusive measurement technique that is suitable for high spatial resolution boundary-layer-resolved velocity measurements [7-9]. In the current implementation, a phosphorescent supramolecule is premixed in the water tunnel [10] and is excited (tagged) by a Lambda Physik LPX 210i XeCl 308 nm UV excimer laser, which turns it into a long-lifetime tracer [11]. The tagging pattern is generated by passing the laser beam through a combination of cylindrical lenses and beam blockers to produce a series of thin parallel lines, normal to the flow, as depicted in Figure 4. A pco.pixelfly CCD camera interrogates the tagged regions twice with a prescribed time delay to form an image pair. Cross-correlation of this image pair provides the displacement vector component normal to the tagging lines [12]. The extracted displacement field from the image pair, along with the known time delay, yields the estimate of the velocity field across the tagged region. In the present study, a total of 14 MTV lines with a streamwise spacing of $0.16d$ are used to measure the streamwise velocity component. The spacing of the velocity measurement points along each tagging line (i.e. the spatial resolution in *y*-direction in Figure 4) is 82 μm ($0.006d$), which is the same as the images' pixel spacing.

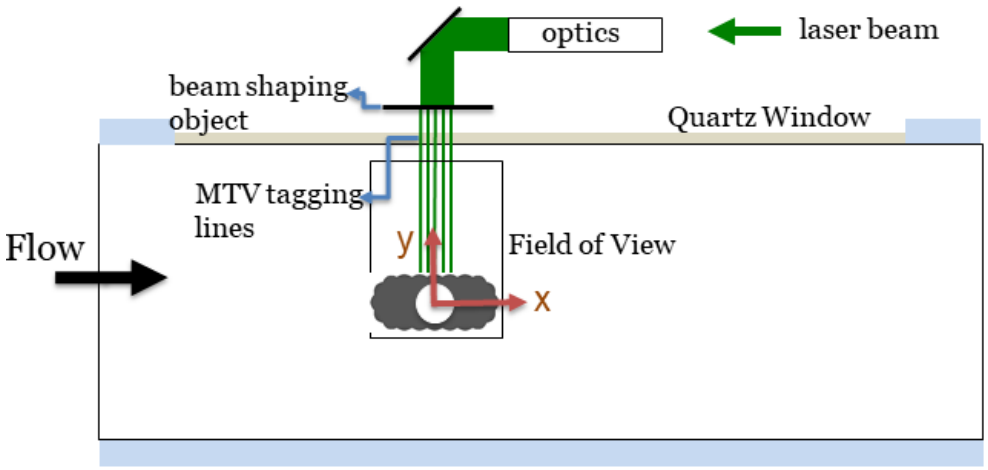

Figure 4. A schematic of the top view of the optical system and the tunnel test section.

Force measurements are carried out using an ATI mini 40 six-component force/torque sensor, which we have previously employed in a number of studies [13-15]. This force transducer has a specified range of 20 N and an instantaneous-reading resolution of 5 mN. Figure 5 shows a schematic of the force measurement setup. In this setup, a closed-loop stepper motor with encoder controls the angular position of the force sensor, and hence the angle of attack of the model, with an angular resolution of 0.02°. This assembly is installed on a motorized translation stage that allows for adjustment of the transverse position of the model (but is not used in the present experiments). The whole force measurement setup is mounted on a rigid structure assembled around, but not connected to, the water tunnel to prevent the transfer of any possible vibrations from the tunnel to the force measurement setup. The transverse component of the planar force vector in the $x-y$ plane (F_y in Figure 1), which is of primary interest, is measured over angles of attack ranging from -2.5° to 2.5° in 0.5° increment for the smooth and 3D model geometries at Re_d numbers of interest.

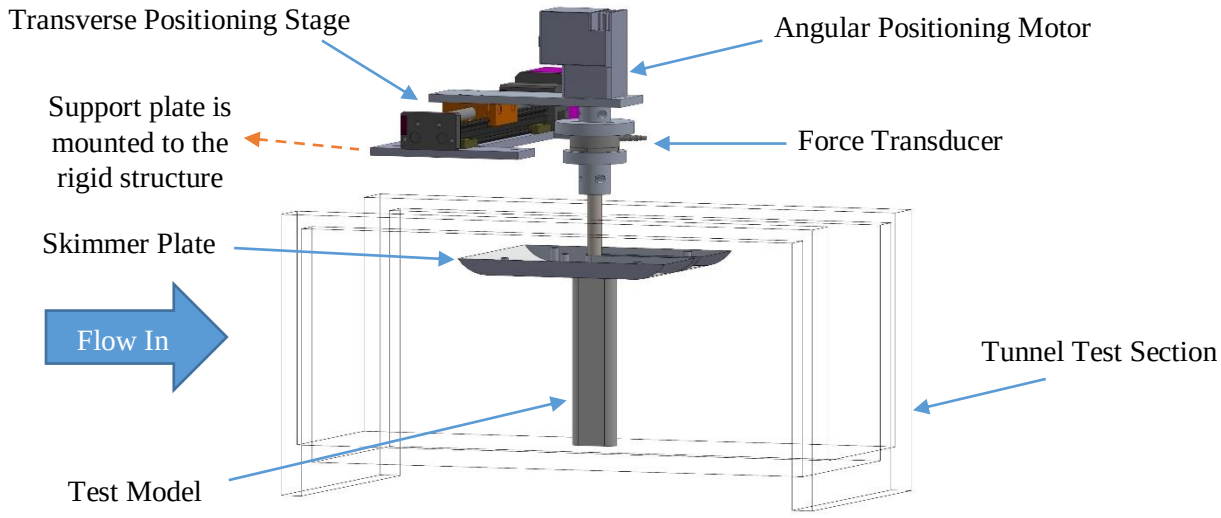

Figure 5. A schematic of the force measurement setup. The setup's support plates are mounted on a structure not shown in the figure.

To account for drift in the output of the load cell, which is the largest contributor to the uncertainty of the force measurements, the sensor output is recorded with the flow off before and after each measurement. The resulting pair of bias voltages are linearly interpolated to estimate and subtract the drift from the measured time series. The overall, uncertainty of the mean F_y force is found to be ~2.6 mN for a single realization of force measurements. Since this value is comparable to the magnitude of the normal force itself (or even larger in some cases, especially at the lower values of Re_d), each measurement is repeated 4 to 16 times, depending on the case, and the results are averaged to reduce the uncertainty. During each realization, force measurement is carried out at a sampling rate of 5 kHz for 120 s, corresponding to a convective time scale of 530 d/U_∞ for Re_d = 1,100, 896 d/U_∞ for Re_d = 1,800 and 1192 d/U_∞ for Re_d = 2,400.

The measurements are performed at Re_d = 1,100 and 2,500, corresponding to $U_\infty = 6.5$ cm/s and 14.8 cm/s respectively, at water temperature of 25°C, where freestream turbulence level of the tunnel is found to be below 1.5% and 1% for the aforementioned Reynolds numbers, respectively. The time delay Δt between the two MTV images (i.e. "un-delayed" and "delayed" images) is set to 7 ms for Re_d = 1,100, and 5 ms for Re_d = 2,500. The exposure time of the images is 700 μs and 500 μs for the lower and higher Reynolds numbers, respectively. For all the cases, 292.6 s-long time series are acquired at a sampling rate of 7 Hz. The duration of the time series corresponds to a convective time scale of 1242 d/U_∞ for Re_d = 1,100 and 2977 d/U_∞ for Re_d = 2,500. Uncertainty analysis for the mean and RMS velocity measurements are reported in Table 1, where "max" refers to the largest uncertainty, and "average" to the mean uncertainty value over the entire measurement domain. For the 3D geometry, measurements are done at two spanwise planes corresponding to sections A-A and B-B in Figure 3. These cases are indicated as 3Dp and 3Dv respectively, where the p and v in the notation signify the presence of a peak and a valley, respectively, at the cylinder's leading edge. The corresponding 2D model cases are denoted as 2Dp and 2Dv, respectively.

Table 1 - Uncertainty of velocity measurements

		$Re_d = 1{,}100$	$Re_d = 2{,}500$
Mean velocity convergence	average	$2.5 \times 10^{-3} U_\infty$	$1.3 \times 10^{-3} U_\infty$
	max	$1.72 \times 10^{-2} U_\infty$	$9.3 \times 10^{-3} U_\infty$
RMS velocity convergence	average	$1.8 \times 10^{-3} U_\infty$	$9 \times 10^{-4} U_\infty$
	max	$1.22 \times 10^{-2} U_\infty$	$6.5 \times 10^{-3} U_\infty$

IV. Results and Discussion

A. Boundary-Layer Characteristics: Mean Separation Zone Boundary

The majority of galloping literature on rectangular cylinders covers the Reynolds number range of $Re_d > 10^4$, mainly focusing on sharp-corner cylinders. For this geometry, separation occurs at the front corners for both boundary layers on the top and the bottom surfaces, and it has been shown that galloping instability can be expected if the separated shear layer does not reattach on the flow-facing side [16]. Additionally, it has been hypothesized recently in [4-5] that the reattachment condition is a necessary but not sufficient condition for galloping stability. Specifically, surface pressure measurements were used in [4-5] to reason that the reattached shear layer must also shrink in size with AoA increase for the cylinder to be stable. On the other hand, due to the open separation on the top side of the cylinder, as the AoA increases, the shear layer behavior on this side does not have a significant effect on the galloping instability. The current study, however, is conducted on cylinders with a baseline geometry that has fully-round corners, which significantly changes the separation behavior of the boundary layer. In addition, it has been observed that with such corner rounding, the shear layer behavior on both sides of the cylinder can affect the galloping instability, and that Re_d can significantly affect this behavior [17]. Therefore, the present

study examines the flow on both sides of the cylinder, and how it is affected by the surface topology and Reynolds number.

The present work focuses on analyzing the separation zone boundary for the different cylinder geometries. This boundary is obtained by identifying the zero-crossing location of each mean velocity profile to delineate the border surrounding the reverse-flow region. A second-order polynomial fit is applied to these locations to capture the shape of the boundary (see Figure 6). The resolution of the data in the immediate vicinity of the wall does not allow exact pinpointing of the separation and reattachment locations (an issue that will be addressed in the future). However, these locations can be reasonably estimated from extrapolation of the separation zone boundary.

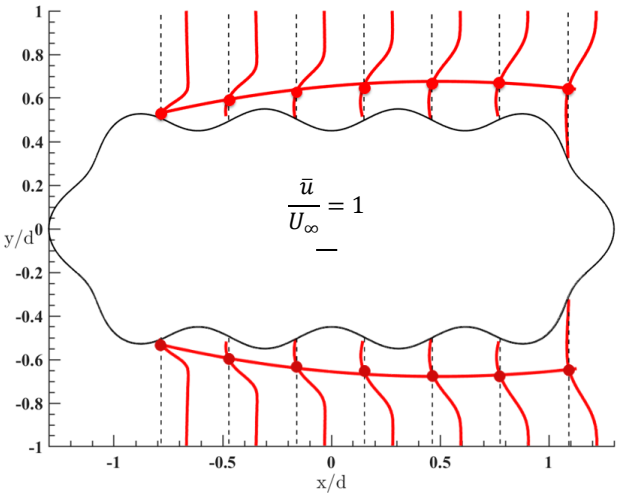

Figure 6. Boundary layer mean velocity profiles on the cylinder with 2D surface topology-peak at the LE. Zero-crossing locations are shown in circles along with their second-order polynomial fit. Flow is from left to right. The velocity scale is indicated on the plot with a horizontal black line.

The separation zone boundary of the smooth cylinder at two Reynolds numbers, $Re_d = 1{,}100$ and $Re_d = 2{,}500$, and three different angles of attack is shown in Figure 7. At zero AoA, the flow remains attached on the lateral surfaces of the cylinder at the low Re_d, within the measurement resolution, but at the high Re_d there is a very thin closed-separation bubble. At higher angles-of-attack, separation occurs on the top side of the cylinder at both Reynolds numbers downstream of the LE round-corner. At $Re_d = 2{,}500$, the separation zone boundary exhibits more curvature with the shear layer appearing to almost reattach at the TE at $\alpha = 2°$. This suggests that the separation bubble remains closed as α is increased from zero, with the bubble opening at $\alpha \approx 2°$. In contrast, for $Re_d = 1{,}100$, once separation occurs, it seems that the bubble remains open. On the bottom side of the cylinder, the flow remains attached as α increases, which should lead to an increase of the pressure on the bottom side with increasing AoA. Thus, the bottom surface is expected to contribute to increasing lift with AoA. A similar contribution to lift is expected from the top surface prior to opening of the separation bubble, with the latter reversing the trend. Moreover, given the tendency of the shear layer on the top side of the cylinder to reattach with increasing Re_d, the top surface contribution to positive lift is anticipated to increase with Re_d.

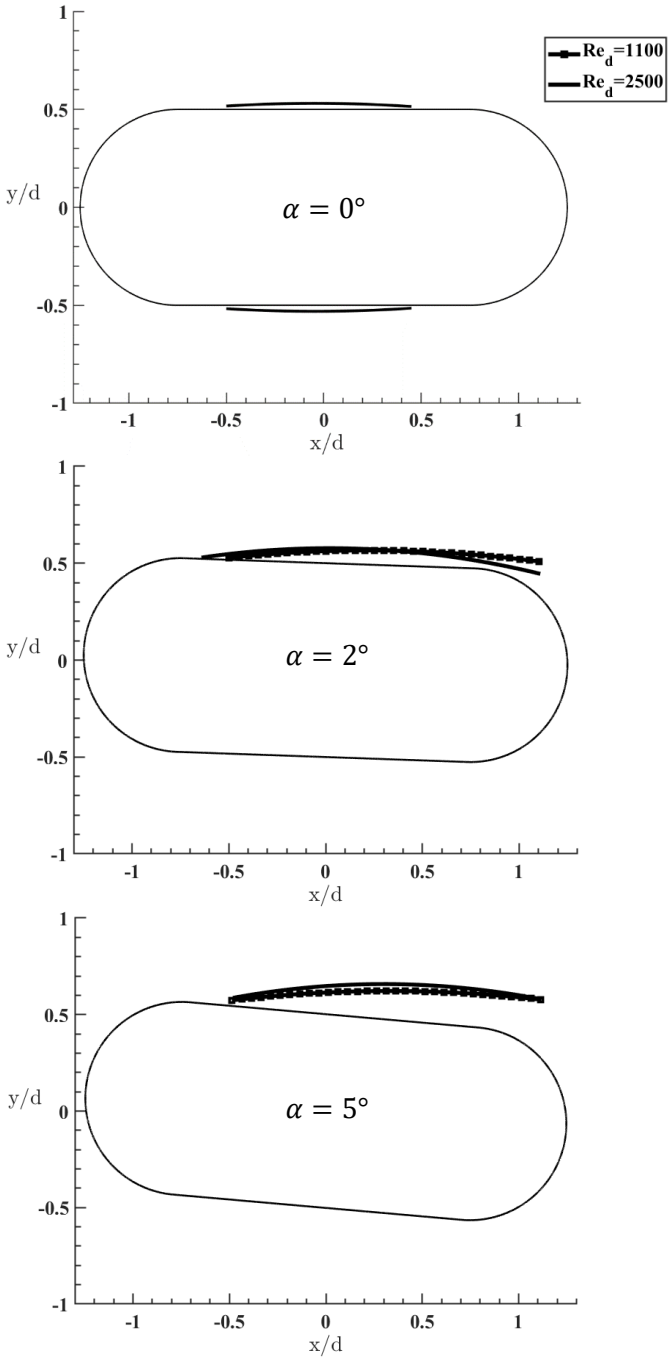

Figure 7. Comparison of the mean separation zone boundary for the smooth cylinder at $\alpha = 0°$ (top), $\alpha = 2°$ (middle), and $\alpha = 5°$ (bottom) for Re_d=1,100 and 2,500.

Noting that $C_l \approx -C_y$ for small α, the above inferences are consistent with the $C_y - \alpha$ curves of the same cylinder geometry from Feero *et al.* [4-5] (see Figure 8-left). Specifically, all curves exhibit a decrease of C_y with AoA for small α values (i.e increasing C_l with α). Moreover, a minimum develops in the $C_y - \alpha$ behavior beyond a certain Reynolds number. This minimum corresponds to a switch in the trend of C_y with α, which *might* be connected to the presence of a closed separation bubble at small AoA that becomes open beyond the α value corresponding to the minimum C_y. The absence of a minimum in C_y at the lowest Re_d *might* be indicative of the inability of a closed bubble to form below a certain Reynolds number.

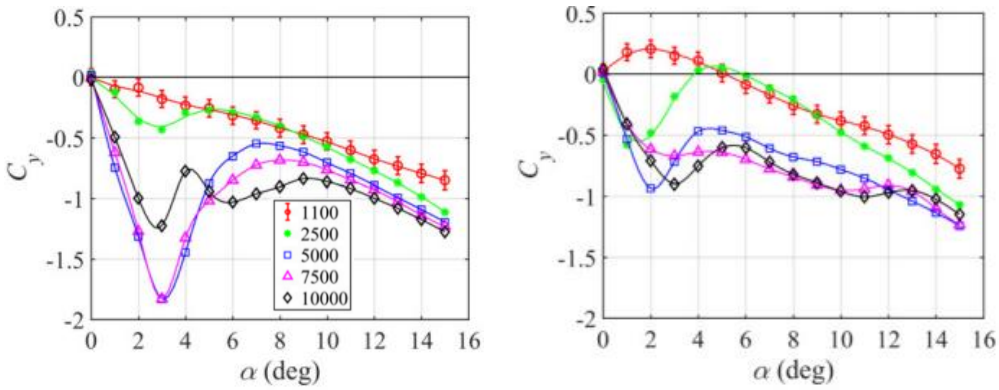

Figure 8. Galloping force characteristics of the smooth cylinder (left) and the cylinder with 3D surface topology (right) reported in [4-5] in a different test facility. Legend shows Re_d values.

Separation zone boundary for the 2Dp and 3Dp cylinders with surface topology peak at the LE is depicted in Figure 9. Focusing on the results of the 2Dp geometry at $\alpha = 0°$, at the low Re_d, the boundary layer separates downstream of the first bump located along the LE corner of the baseline geometry. The separation location seems uninfluenced by Re_d. On the other hand, while the separated shear layer remains open at the low Reynolds number for the 2Dp geometry, the shear layer reattaches upstream of the last lateral topology bump at the high Re_d. Addition of three-dimensionality to the surface topology results in decreasing the lateral thickness of the separation zone by curving the shear layer towards the surface.

To connect the features of boundary layer separation/reattachment to galloping instability, it is important to examine how these features change with increasing AoA. Referring to Figure 9 (middle row), the separation remains open on the top and the bottom of the 2Dp cylinder at $Re_d = 1{,}100$ when α is increased to 2°. This behavior is reminiscent of that of the sharp-corner, low-side-ratio rectangular cylinders, which are unstable to galloping (Parkinson [16]), and hence one may expect instability to galloping for this cylinder at the low Re_d. As the angle of attack is increased further to 5 degree (Figure 9, bottom), the shear layer reattaches on the bottom side, suggesting pressure recovery on the bottom side, positive lift, and a switch of the $C_y - \alpha$ slope sign at some angle $2° < \alpha < 5°$. Increasing Re_d to 2,500, causes the separated shear layer to remain reattached on the top surface of the 2Dp cylinder up to $\alpha = 2°$, somewhere upstream of the final lateral bump on the top surface (upstream of the round corner of the trailing-edge of the base geometry). Further increase to $\alpha = 5°$, leads to opening of the separation bubble. In contrast, on the bottom side of the 2Dp case, the flow separates downstream of the first, and reattaches upstream of the last bump of surface topology at all measured AoAs. The separation bubble on the bottom side is not shrinking significantly with α; however, considering the reattachment of the shear layer on the top side of the cylinder, a stronger suction pressure (and hence higher lift) is expected relative to the same geometry at the lower Reynolds number. Hence, increasing the Reynolds number is hypothesized to lead to galloping stability for the 2Dp cylinder.

In Figure 9, for all AoA, the three-dimensionality of the topology leads the separated shear layer on both sides of the 3Dp cylinder to move closer to the surface compared to the 2Dp case. Due to the associated higher curvature of the shear layer on the top surface, higher suction pressure relative to the 2Dp case is expected; i.e. promoting an increase in lift and stability to galloping. On the bottom side, the shear layer remains reattached and the separation bubble's length shrinks with increasing α (in fact no bubble is detected within the measurement resolution at $\alpha = 5°$ and $Re_d = 1{,}100$). This behavior is anticipated to increase the pressure recovery on the bottom side of the cylinder with α, contributing further to the increase in lift and stability to galloping. It should be noted, however, that the behavior of the 3D cylinder as a whole cannot be solely determined by looking at a single cross section.

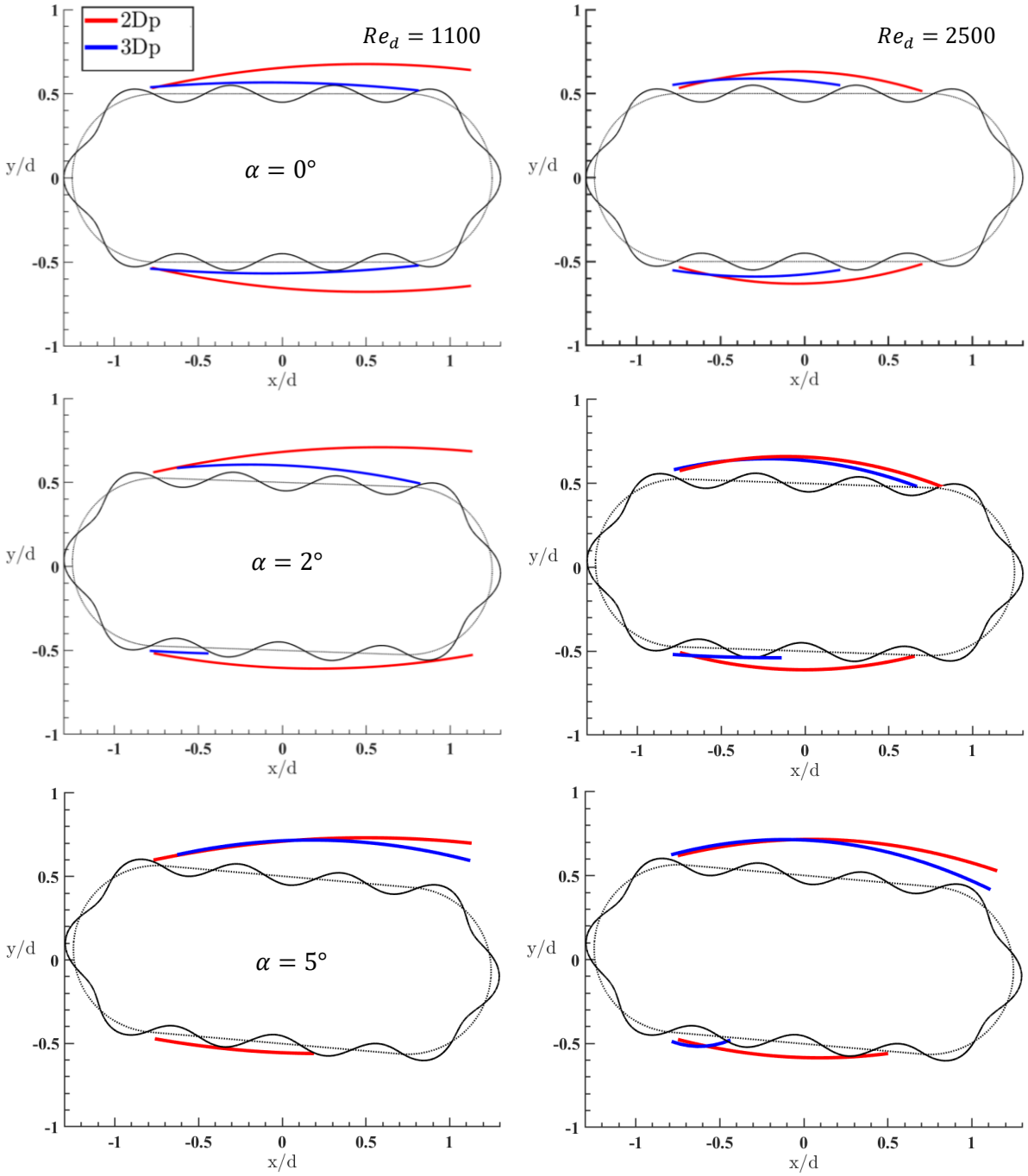

Figure 9. Comparison of the mean separation zone boundary for the cylinders with surface topology with peak at the LE at different angles of attack (different rows) and Reynolds numbers (different columns). 2D and 3D geometry is depicted in red and blue, respectively.

Overall, for the cylinder with a topology peak at the LE, boundary layer separation occurs for all cases, on both the top and bottom surfaces, downstream of the first bump of the surface topology along the LE corners of the base geometry. The separation is not significantly affected by either three-dimensionality or Reynolds number. However, decreasing Reynolds number makes reattachment of the separated shear layer on the upper surface more difficult; an effect that is expected to decrease the stability to galloping. Additionally, the presence of three-dimensionality keeps the separated shear layers closer to the surface,

promoting reattachment, which is expected to improve galloping stability. If true, this suggests that a lower Reynolds number would be required to destabilize the 3Dp in comparison to the 2Dp geometry.

Results for the cylinders with surface topology valley at the LE are shown in Figure 10. The difference in the mean separation zone boundary of the 2Dv and 3Dv cases for all angles of attack and both Reynolds numbers is not significant. Also, for all cases, the separation zone boundary on the bottom is generally very thin, and, with the exception of the zero AoA at the low Reynolds number, the shear layer is reattached. Thus, the flow generally follows the baseline shape of the cylinder on the bottom side, which would likely lead to increased bottom surface pressure with AoA, contributing to stability to galloping. On the top surface, the flow separates downstream of the first surface topology bump, located downstream of the round LE corner of the base geometry for all cases. Therefore, in comparison to the case with a peak at the LE, when a valley is present at the LE, separation occurs later.

At $Re_d = 1{,}100$, the flow forms an open separation on the top side at all AoA. In comparison, at $Re_d = 2{,}500$, reattachment occurs at $\alpha = 0°$ and possibly $\alpha = 2°$ (the latter is difficult to ascertain with the present near-wall measurement resolution). Overall, as in the case of the 2Dp and 3Dp cylinders, increasing the Reynolds number promotes shear layer reattachment, increasing the curvature of the separation bubble and/or the shear layer, which is expected to promote the overall stability to galloping, as discussed previously.

The above results lead to some interesting observations. Comparing the 2Dp versus the 2Dv geometry, in both cases separation occurs over a topology peak. This peak, or bump, in the case of the valley configuration (and the specific wavelength λ_s used here) is placed farther downstream (along the flat side of the baseline geometry) than the corresponding bump when a peak is at the LE (which is along the round corner of the baseline geometry). Thus, separation is delayed for the valley case, and the flow "hugs" the shape of the baseline geometry more closely; i.e. the 2Dv cross-section is more "streamlined" than that of the 2Dp. For the latter, the presence of the bump over which the flow separates at the LE corner leads to flow behavior similar to that of bluff bodies, with open separation on both sides of the cylinder at low Reynolds number. This is the type of behavior that is known to lead to galloping in literature (Parkinson [16]). The presence of three-dimensionality retains this basic flow behavior, except the topology amplitude variation along the spanwise direction is found to lead to the separation boundary zone remaining closer to the surface; an effect that should be favorable to galloping stability. Additionally, the hypothesized destabilizing effect of the geometry with a peak at the LE is reduced with increasing Re_d.

B. Direct Force Measurements: $C_y - \alpha$ Characteristics

As mentioned in the introduction, while the force results of Feero *et al.* [4-5] were for a cylinder with a topology geometry similar to the one used in this work, those measurements were performed in a wind tunnel facility with different free-stream turbulence level, cylinder aspect ratio and flow blockage. To ensure a direct connection between the observed boundary layer behavior and the force characteristics of the cylinders, direct force measurements are performed on the same cylinders in the same water tunnel facility used for the velocimetry measurements discussed in Section IV.A. It should be noted that these force measurements are still ongoing and only some preliminary results are presented here.

The normal average force coefficient (C_y) measured for the 3D cylinder is presented in Figure 11 as a function of AoA for Re_d = 1,100, 1,800 and 2,400. It is observed that as Re_d decreases, the negative slope of the C_y curve becomes smaller in magnitude, and at low enough Re_d value ($Re_d \approx 1{,}800$) transitions into a positive slope. This indicates that decreasing Re_d has a destabilizing effect on galloping instability for the 3D geometry, as previously reported by Feero *et al.* [4-5], and hypothesized based on the MTV data in Section IV.A.

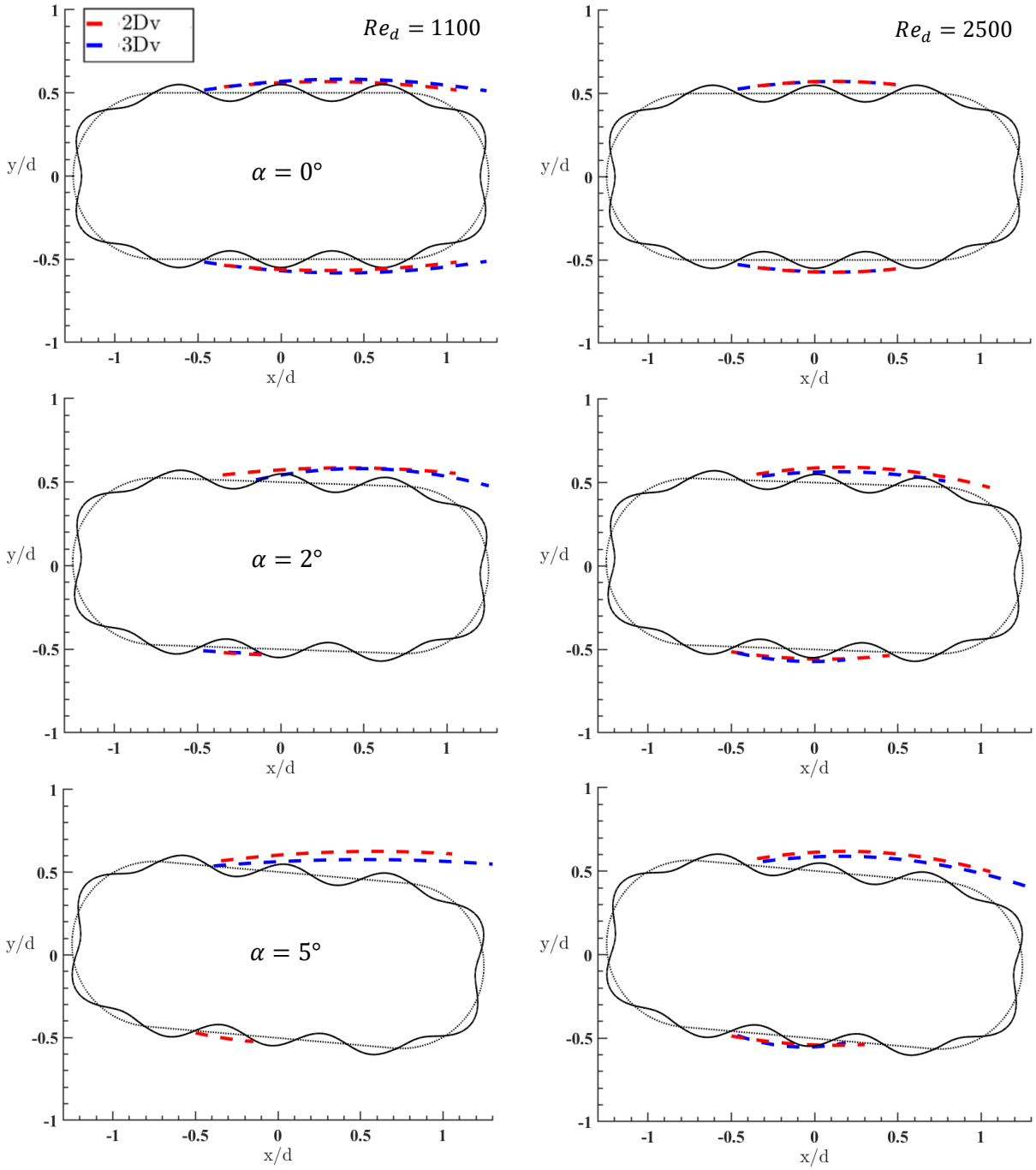

Figure 10. Comparison of the mean separation zone boundary for the cylinders with surface topology with valley at the LE at different angles of attack (different rows) and Reynolds numbers (different columns). 2D and 3D geometry is depicted in red and blue, respectively.

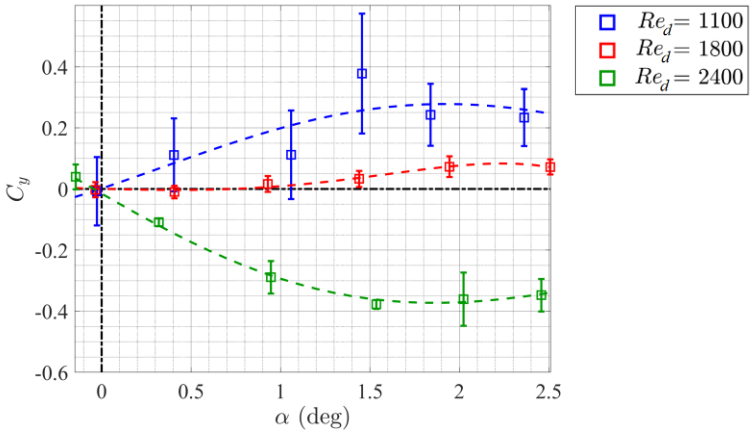

Figure 11. Comparison of the $C_y - \alpha$ behavior for the cylinder with 3D surface topology for Re_d = 1,100, 1,800 and 2,400.

Figure 12 summarizes the slope of C_y versus α curve at zero AoA, $\partial C_y/\partial\alpha|_{\alpha=0}$, for the smooth cylinder and the one with 3D surface topology as a function of Re_d . For reference, the figure also contains data from Feero *et al.* [4-5]. Consistent with the latter study, it is observed that at Re_d = 2,400, the addition of surface topology results in a larger negative slope of the C_y curve at zero AoA, which makes the cylinder more stable to galloping. However, at Re_d = 1,100, the 3D surface topology has the opposite, destabilizing, effect by producing a positive slope at zero AoA. This effect is also consistent with the data from Feero *et al.* [4-5]. It should be noted that based on the currently available measurements for the smooth cylinder at Re_d = 1,100, the extent of the uncertainties hinders the extraction of a reliable slope, and hence no data point is shown for this case in Figure 12.

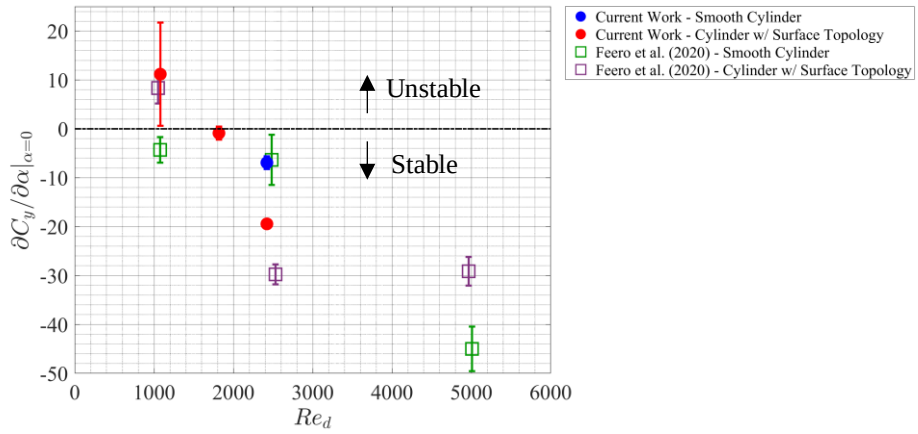

Figure 12. Effect of 3D surface topology on the galloping stability criterion at $\alpha = 0°$ with comparison to the smooth geometry. The experimental data of Feero *et al.* [4-5]) are included for reference.

Additional force measurements are ongoing on the 2D valley-leading and 2D peak-leading surface topologies, and they will be compared to the current results for smooth and 3D cylinders in future work.

V. Conclusion

Motivated by galloping of Precision Airdrop Systems, effects of surface topology on the aerodynamics of rectangular cylinders with round corners are investigated systematically. The investigation considers variation of the surface topology along the perimeter only (2D cylinders) as well as when including spanwise variation in the topology (3D cylinder). For the 2D cases, two configurations are examined with cross-sections similar to those of the 3D cylinder at two spanwise locations corresponding to a peak and a valley of the topology at the leading edge (denoted as 2Dp and 2Dv respectively). Single-component molecular tagging velocimetry is carried out on these cylinder models in a water tunnel at $Re_d = 1{,}100$ and $2{,}500$ and three different angles of attack. Complementary force measurements are also reported, for some of the models and $Re_d = 1{,}100, 1{,}800$ and $2{,}400$, to determine the galloping instability of these models.

Overall, it is found that the presence of the topology could cause the boundary layer on the top side of the cylinder to separate earlier (i.e. farther upstream) compared to the baseline (smooth) geometry. For the specific geometries considered in the present work, this occurred for the 2Dp case and when measuring in a spanwise plane where a peak is present at the leading edge for the 3D geometry. Drawing on present understanding in literature on galloping, it is hypothesized that the promotion of earlier separation due to the presence of surface topology has a destabilizing influence on galloping. This is opposed by the stabilizing effect of the reattachment of the shear layer, which is found to be promoted by the presence of spanwise variation in the topology (3D geometry) and increasing Reynolds number. The Reynolds number effect inferred from the separation and reattachment characteristics of the top-surface shear layer is found to be consistent with the present force data, and the earlier work of Feero *et al.* [4-5] in a different flow facility.

Acknowledgements

This work is supported by Army Research Office (ARO) grant number W911NF-17-1-0153. The views and conclusions contained in this document are those of the authors and should not be interpreted as representing the official policies, either expressed or implied, of ARO or the U.S. Government. The U.S. Government is authorized to reproduce and distribute reprints for Government purposes notwithstanding any copyright notation herein.

References

[1] Blevins, R. D., "Flow-induced vibration," New York, Van Nostrand Reinhold Co., 1977.

[2] Bergeron, K., Ecklebe, D., McClure, K., Johari, H., Curlett, T. and Pitman, B., "Parachute suspension line drag analysis," AIAA paper 2009-2982, 20th AIAA Aerodynamic Decelerator Systems Technology Conference and Seminar, 4-7 May, Seattle, WA, 2009.
doi: 10.2514/6.2009-2982

[3] Siefers, T., Greene, K., McLaughlin, T. and Bergeron, K., "Wind and water tunnel measurements of parachute suspension line," AIAA paper 2013-0064, 51st AIAA Aerospace Sciences Meeting including the New Horizons Forum and Aerospace Exposition, 7-10 January, Grapevine, TX, 2013.
doi: 10.2514/6.2013-64

[4] Feero, M. A., Naguib, A. M. and Koochesfahani, M. M., "Surface topology effects on the transverse galloping behavior of rectangular cylinders," 11th International Symposium on Turbulence and Shear Flow Phenomena (TSFP 11), Southampton, UK, July 30 to August 2 2019.

[5] Feero, M. A., Naguib, A. M. and Koochesfahani, M. M., "Effect of surface topology on the galloping instability of rectangular cylinders," International Journal of Heat and Fluid Flow, Vol 86, 2020, p. 108721
doi: 10.1016/j.ijheatfluidflow.2020.108721

[6] Kalan, K., Feero, M. A., Naguib, A. M. and Koochesfahani, M. M., "Influence of surface topology on boundary layer and near-wake behavior of rectangular cylinders," AIAA paper 2020-2034, AIAA SciTech Forum, 6-10 January, Orlando, FL, 2020.
doi: 10.2514/6.2020-2034

[7] Olson, D. A., Katz, A. W., Naguib, A. M., Koochesfahani, M. M., Rizzetta, D. P., and Visbal, M. R., "On the challenges in experimental characterization of flow separation over airfoils at low Reynolds number," Experiments in Fluids, Vol. 54, No. 2, 2013, p. 1470.
doi: 10.1007/s00348-013-1470-1

[8] Hammer, P., Pouya, S., Naguib, A. M., and Koochesfahani, M. M., "A multi-time-delay approach for correction of the inherent error in single-component molecular tagging velocimetry," Measurement Science and Technology, Vol. 24, No. 10, 2013, p. 105302.
doi: 10.1088/0957-0233/24/10/105302

[9] Olson, D. A., Naguib, A. M., and Koochesfahani, M. M., "Measurement of the wall pressure and shear stress distribution using molecular tagging diagnostics," Experiments in Fluids, Vol. 56, No. 8, 2015, p. 171.
doi: 10.1007/s00348-015-2039-y

[10] Gendrich, C.P., Koochesfahani, M.M. and Nocera, D.G., "Molecular tagging velocimetry and other novel applications of a new phosphorescent supramolecule," Experiments in Fluids, Vol. 23, No. 5, 1997, pp. 361-372.
doi: 10.1007/s003480050123

[11] Koochesfahani, M. M., and Nocera, D. G., "Molecular Tagging Velocimetry," In: Tropea, C., Yarin, A. L., Foss, J. F. (eds) Handbook of Experimental Fluid Dynamics, Chap 5.4, Springer, Berlin Heidelberg, 2007, pp. 362–382.
doi: 10.1007/978-3-540-30299-5_5

[12] Gendrich, C.P. and Koochesfahani, M.M., "A spatial correlation technique for estimating velocity fields using molecular tagging velocimetry (MTV)," Experiments in Fluids, Vol. 22, No. 1, 1996, pp. 67-77.
doi: 10.1007/BF01893307

[13] Hammer, P. R., Olson, D. A., Visbal, M. R., Naguib, A. M. and Koochesfahani, M. M., "Joint Computational-Experimental Investigation of Harmonically Pitching Airfoil Aerodynamics in Uniform-Shear Approach Flow," AIAA Journal, Vol 57, No. 8, 2019, pp. 3290-3298.
doi: 10.2514/1.J058232

[14] Hamedani, B. A., Naguib, A. M. and Koochesfahani, M. M., "Reynolds Number Effect on Lift Characteristics of an Airfoil Translating Across a Non-uniform Approach Flow," AIAA paper 2019-0639, AIAA SciTech Forum, 7-11 January, San Diego, CA, 2019.
doi: 10.2514/6.2019-0639

[15] Albrecht, M. B., Naguib, A. M. and Koochesfahani, M. M., "A Study of the Aerodynamics of a Low Reynolds Number Airfoil Translating Across a Uniform-Shear Approach Flow," AIAA paper 2019-2157, AIAA SciTech Forum, 7-11 January, San Diego, CA, 2019.
doi: 10.2514/6.2019-2157

[16] Parkinson, G., "Phenomena and modeling of flow-induced vibrations of bluff bodies," Progress in Aerospace Sciences, Vol 26, No. 2, 1989, pp. 169-224.
doi: 10.1016/0376-0421(89)90008-0

[17] Carassale, L., Freda, A. and Marrè-Brunenghi, M., "Experimental investigation on the aerodynamic behavior of square cylinders with rounded corners," Journal of Fluids and Structures, Vol 44, 2014, pp. 195-204.
doi: 10.1016/j.jfluidstructs.2013.10.010